The critical current I_c is proportional to the coupling strength κ, which describes the overlap of the wave functions Ψ_1 and Ψ_2 within the insulating layer. The relationship is given by

$$I_\mathrm{c} = \frac{4e\kappa V n_\mathrm{s}}{\hbar} \quad , \tag{2.4}$$

where V represents the volume of the superconducting electrode and e denotes the elementary charge of an electron. We assume that the Cooper pair density n_s of the two superconductors S_1 and S_2 is identical, meaning $n_\mathrm{s1} = n_\mathrm{s2} = n_\mathrm{s}$.

The gauge-invariant phase difference refers to the phases θ_1 and θ_2 of the respective electrodes at the boundary of the insulating layer (positions 1 and 2, see figure 2.1). Taking into account possible external electromagnetic fields within the barrier, the general form using the vector potential $\mathbf{A}$ is given by [Gro16]

$$\varphi(\mathbf{r},t) = \theta_2(\mathbf{r},t) - \theta_1(\mathbf{r},t) - \frac{2\pi}{\Phi_0} \int\limits_1^2 \mathbf{A}(\mathbf{r},t) \cdot \mathrm{d}\mathbf{l} \quad . \tag{2.5}$$

Assuming a constant supercurrent density J_s across the junction, taking the time derivative of equation (2.5) yields the **second Josephson equation** [Jos65]

$$\frac{\partial \varphi}{\partial t} = \frac{2\pi}{\Phi_0} V \quad . \tag{2.6}$$

The first of the two above-mentioned operating modes describes the zero-voltage state, i.e. $I < I_\mathrm{c}$. Here, the entire injected current is carried by Cooper pairs, so $I = I_\mathrm{s} = \mathrm{const}$. As a result, φ is constant over time, which, according to equation (2.6), leads to $V = 0$. This is known as the *dc Josephson effect*.

For $I > I_\mathrm{c}$ however, Cooper pairs begin to break up into quasiparticles which carry that portion of the current leading to a voltage drop V. According to the second Josephson equation, the phase φ becomes time dependent, and after integration one obtains

$$\varphi = \frac{2\pi}{\Phi_0} V t + \varphi_0 = w_\mathrm{J} t + \varphi_0 \quad \text{with} \quad w_\mathrm{J} = \frac{2\pi}{\Phi_0} V \quad . \tag{2.7}$$

Thus, if we insert equation (2.7) into equation (2.3), we observe that the current I_s oscillates with the *Josephson frequency* $f_\mathrm{J}/V = w_\mathrm{J}/(2\pi V) = 1/\Phi_0 \approx 483.6\,\mathrm{MHz/\mu V}$. Accordingly, this phenomenon is referred to as the *ac Josephson effect*.

2.1.2 Josephson Junctions in a Magnetic Field

To motivate the structure of a dc-SQUID, it is essential to first investigate the current behavior of an extended Josephson junction in the presence of an external magnetic field. So far, all previous formulae apply for point-like junctions, assuming a spatially constant phase difference φ and Josephson current density J_s across the junction area. This is not the case for three-dimensional (extended) junctions with a length L and width W. The *Josephson penetration depth* λ_J is a quantity used to classify an extended junction as short $(W, L \leq \lambda_J)$ or long $(W, L \geq \lambda_J)$ and is defined as [Wei69]

$$\lambda_J = \sqrt{\frac{\Phi_0}{2\pi\mu_0 J_c t_B}} \quad . \tag{2.8}$$

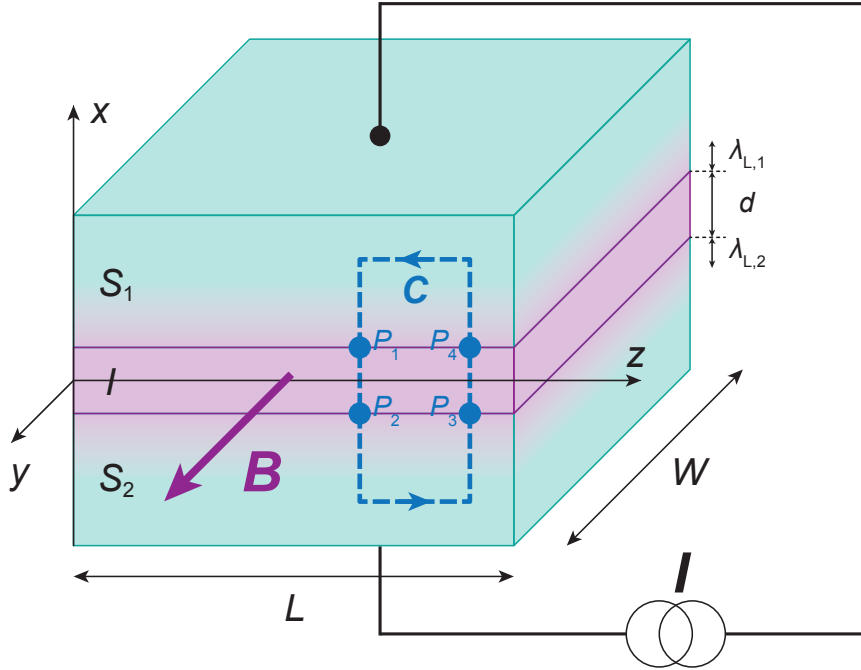Here, the magnetic thickness is defined as $t_B = d + \lambda_{L,1} + \lambda_{L,2}$, where d is the geo-

Figure 2.3: Short Josephson junction connected to a current source in the presence of an external B-field in y-direction, parallel to the junction area. Inside the electrodes the magnetic field decays exponentially according to the London penetration depths $\lambda_{L,1}$ and $\lambda_{L,2}$, visually shown by the purple color gradient. The closed contour C is used to derive expressions for the spatially dependent phase difference φ and current density J_s.

metric thickness of the isolator and λ_{L} the London penetration depth of respective superconducting electrode. It describes how far an external magnetic field penetrates both superconducting electrodes if applied parallel to the junction area, as depicted in figure 2.3. The respective London penetration depths are $\lambda_{\mathrm{L,1}}$ and $\lambda_{\mathrm{L,2}}$ and $J_{\mathrm{c}} = I_{\mathrm{c}}/(WL)$ is the critical current density. This distinction is needed to determine whether the magnetic self-field generated by the supercurrent is negligible in comparison to the external field (short junctions) or not (long junctions). Within the scope of this thesis, we only use short junctions.

To analyze the current and phase distribution of such a junction we consider the setup shown in figure 2.3. A short junction is connected to a current source and is penetrated by an external B-field in y-direction, parallel to the junction area. Now, obtaining an expression for the phase requires a similar approach as the calculation for the quantized flux, where we assumed that the phase changes by $2\pi n$ around a closed loop. Here, we again integrate over a closed contour C, with the points $P_1 - P_4$ marking the transitions between superconductor and isolator. Using equation 2.5, we find

$$\frac{\partial \varphi}{\partial z} = \frac{2\pi}{\Phi_0} B_{\mathrm{y}} t_{\mathrm{B}} \quad \text{and} \quad \frac{\partial \varphi}{\partial y} = -\frac{2\pi}{\Phi_0} B_{\mathrm{z}} t_{\mathrm{B}} \quad . \tag{2.9}$$

The magnetic field points in y-direction only, meaning φ will only vary along the z-axis. Integrating the first expression in equation 2.9 then leads to

$$\varphi(z) = \frac{2\pi}{\Phi_0} B_{\mathrm{y}} t_{\mathrm{B}} z + \varphi_0 \quad . \tag{2.10}$$

Here, the integration constant φ_0 represents the phase difference for the case $z = 0$. Inserting equation 2.10 into the first Josephson equation and using $J_{\mathrm{s}} = I_{\mathrm{s}}/WL$ gives

$$J_{\mathrm{s}}(y,z,t) = J_{\mathrm{c}}(y,z) \sin(kz + \varphi_0) \quad \text{with} \quad k = \frac{2\pi}{\Phi_0} B_{\mathrm{y}} t_{\mathrm{B}} \quad . \tag{2.11}$$

If we now assume the critical current density J_{c} to be constant across the junction area, we can integrate equation 2.11 to get a flux-dependent maximum Josephson current

$$I_{\mathrm{s}}^{\mathrm{m}}(\Phi) = I_{\mathrm{c}} \left| \frac{\sin\left(\frac{kL}{2}\right)}{\frac{kL}{2}} \right| = I_{\mathrm{c}} \left| \frac{\sin\left(\frac{\pi\Phi}{\Phi_0}\right)}{\frac{\pi\Phi}{\Phi_0}} \right| \quad , \tag{2.12}$$

where $\Phi = B_{\mathrm{y}} t_{\mathrm{B}} L$ is the total flux threading through the junction. This expression describes the so-called Fraunhofer diffraction pattern, shown in figure 2.4. The result
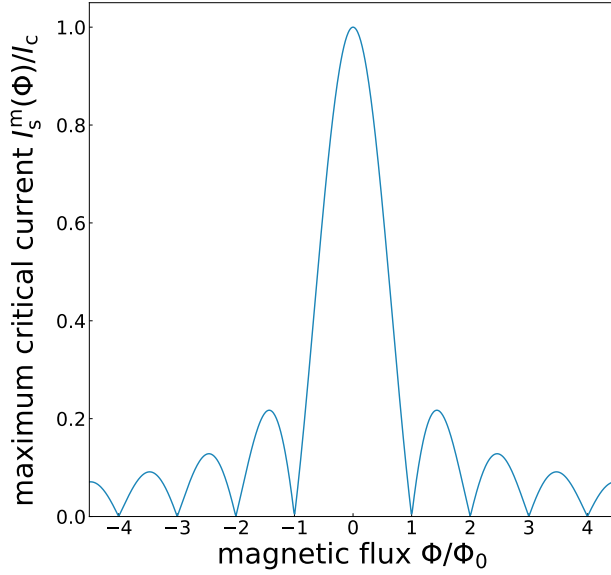
Figure 2.4: Normalized flux-dependent maximum Josephson current $I_s^m(\Phi)$ showing a Fraunhofer pattern. It modulates with the flux quantum Φ_0, peaking at $\Phi = 0$ with subsequent maxima at $\Phi = \pm(\frac{3}{2} + n)\Phi_0$ with $n \in \mathbb{N}_0$. For $\Phi = \pm(n + 1)\Phi_0$ the total net current is zero.

resembles the single slit experiment, where the same pattern is found for the light intensity behind the slit. Here, the analogy works by considering the integral of the critical current density J_c as a transmission function which is constant inside the junction and zero outside.

2.1.3 RCSJ Model

The Fraunhofer pattern describes the flux-dependent current for the case of $I < I_c$, staying in the so-called zero-voltage state. In this regime, only the dc Josephson effect applies as discussed in subsection 2.1.1. Switching to the voltage stage, i.e. $I > I_c$, Cooper pairs start breaking up into quasiparticles if the electric energy eV exceeds the sum of both electrodes' gap energies $\Delta_1(T) + \Delta_2(T)$ [Bar57]. Consequently, at the *gap-voltage*

$$V_g = \frac{\Delta_1(T) + \Delta_2(T)}{e} \tag{2.13}$$

quasiparticles start to cross the tunnel barrier resulting in a steep rise of a resistive normal current I_n. This process also occurs at finite temperatures for $k_B T > \Delta_1(T) + \Delta_2(T)$, leading to a reduction of I_c as well as V_g. Under a dc current source, the condition $I = I_s + I_n$ must be constantly fulfilled. This results in an oscillating normal current and therefore voltage, since I_s oscillates with f_J according to the ac Josephson effect. According to the second Josephson equation (2.6) the oscillating
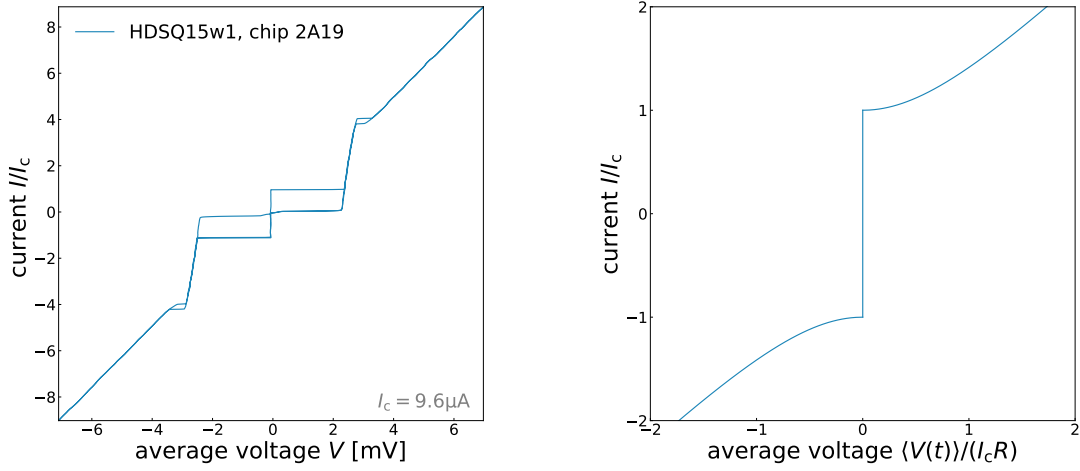
Figure 2.5: Left: Measured IVC of an underdamped junction manufactured in this working group, showing the typical hysteresis. Right: Theoretical IVC of an over-damped junction with a current-voltage shape that is independent of the current sweep direction.

voltage thus causes the term $\mathrm{d}\varphi/\mathrm{d}t$ to vary sinusoidally, causing both I_s and I_n and in turn the resulting voltage to oscillate in a complex manner. As a voltage with such a high frequency cannot be measured, only the time-averaged voltage will be considered in the following discussion.

Now, further increasing the energy of the quasiparticles ($T > T_\mathrm{c}$ and/or $V > V_\mathrm{g}$) leads to a transition into normal-conducting electrons, which exhibit an ohmic dependence. This behavior can be seen in the typical current-voltage-characteristic (IVC) depicted in figure 2.5.

For real junctions, however, one needs to take into account that they are comprised of two electrodes separated by a thin insulating layer, which represent a parallel plate capacitor with the Al-AlO$_\mathrm{x}$ layer being the dielectric material. Therefore, a junction capacitance C needs to be taken into account. A displacement current I_d will flow as a consequence, given we are in the voltage state. Lastly, thermal and 1/f noise cause a small fluctuating current I_f. All these current channels were defined in the so-called Resistively and Capacitively Shunted Junction (RCSJ) model [McC68], [Ste68], which models the total current of a lumped (0-dimensional) junction to a sufficiently high accuracy. A schematic of an effective circuit diagram is shown in figure 2.6 (left). Combining every current channel utilizing Kirchhoff's law leads to the *Basic Junction Equation*, which is defined as [Gro16]
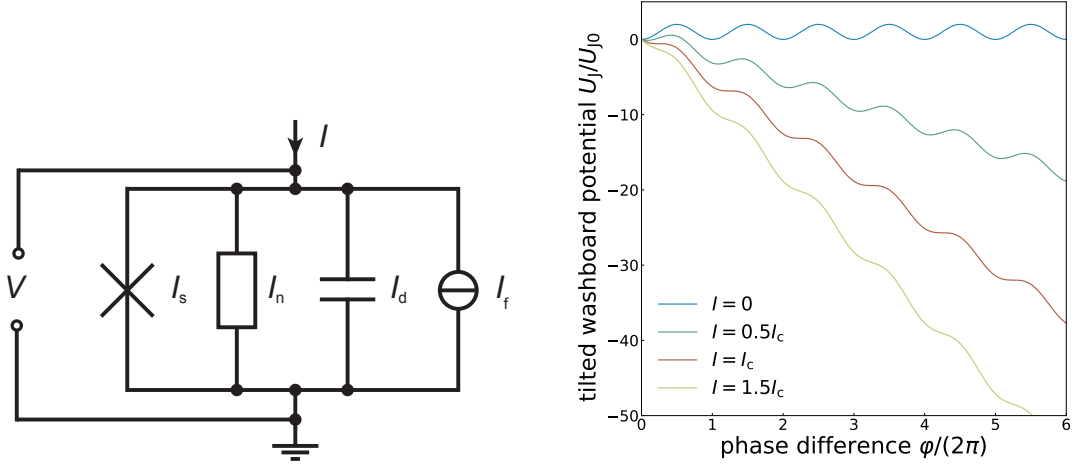
Figure 2.6: Left: Schematic circuit of a lumped Josephson junction with all four current channels connected in parallel, according to the RCSJ model. The junction is represented by the cross symbol on the left, marking the supercurrent I_s. The normal current I_n is realized with a resistance R, while the displacement current I_d and the noise I_f are attributed to a capacitor C and a current source, respectively. Right: Tilted washboard potential for different currents, ranging from 0 to $1.5I_c$. The tilt increases with the injected current I.

$$I = I_s + I_n + I_d + I_f = I_c \sin(\varphi) + \frac{1}{R(V)} \frac{\Phi_0}{2\pi} \frac{\mathrm{d}\varphi}{\mathrm{d}t} + C \frac{\Phi_0}{2\pi} \frac{\mathrm{d}^2\varphi}{\mathrm{d}t^2} + I_f \quad . \tag{2.14}$$

By defining the Josephson coupling energy $U_{J0} = \hbar I_c/(2e)$ and the normalized currents $i = I/I_c$ and $i_f(t) = I_f(t)/I_c$, equation 2.14 can be rewritten to

$$\left(\frac{\hbar}{2e}\right)^2 C \frac{\mathrm{d}^2\varphi}{\mathrm{d}t^2} + \left(\frac{\hbar}{2e}\right)^2 \frac{1}{R(V)} \frac{\mathrm{d}\varphi}{\mathrm{d}t} + \frac{\mathrm{d}}{\mathrm{d}\varphi} \{U_{J0} [1 - \cos\varphi - i\varphi + i_f(t)\varphi]\} = 0 \quad . \tag{2.15}$$

The expression in the curly brackets represents the potential energy in the system U_J, allowing equation 2.14 to be compared to

$$M \frac{\mathrm{d}^2 x}{\mathrm{d}t^2} + \eta \frac{\mathrm{d}x}{\mathrm{d}t} + \nabla U = 0 \quad , \tag{2.16}$$

which describes a particle with mass M and damping η moving inside the potential U. This mechanical analogue therefore allows us to interpret as the equation

of motion for a *phase particle*, where it's motion corresponds to a change of the gauge-invariant phase difference φ within a potential U_{J} [Cla04]. Consequently, it is attributed with a mass $M = (\hbar/(2e))^2 C$ and damping $\eta = (\hbar/(2e))^2 / R(V)$. Figure 2.6 (right) visualizes how this phase particle behaves for different currents I. Given the shape of $U_{\mathrm{J}}(\varphi)$, the potential is referred to as the *tilted washboard potential*.

For $I = 0$, the phase particle will remain within one of the potential minima. As the current increases, however, the potential starts to tilt such that the depth of the minima reduces until it vanishes for $I = I_{\mathrm{c}}$, thus becoming a saddle point. Up until this point, the phase particle can't overcome the potential barrier to move downward, which agrees with the second Josephson equation as the phase difference φ should remain constant on average for $I < I_{\mathrm{c}}$. Further increasing the current and therefore the tilt of the potential causes the phase particle to fall along the potential, resulting in a voltage drop across the junction ($\partial\varphi/\partial t > 0$).

Reversing the current sweep showcases the importance of the particle's mass M and damping η, as they determine if the return path equals the current shape described above or not. For the case of a small mass (small C) and large damping (small R), the phase particle will, due to a lack of momentum and strong damping, come to a halt as soon as minima reappear in the washboard potential by reducing the current below I_{c}. The current path will therefore remain unchanged as I is reduced back to 0, as shown in figure 2.5 (right). Such a junction is consequently called an *overdamped* junction.

The other case describes an *underdamped* junction (figure 2.5 (left)) and involves a large mass (large C) and small damping (large R). This allows the phase particle to continue to move downward as it now carries enough momentum to overcome the arising maxima and minima. The finite voltage drop despite the current being below I_{c} is displayed as the steep quasiparticle current curve, which ends with a return current I_{R} that arises with the recapture of the particle in a minimum. This leads to a hysteretic IVC, as depicted in figure 2.5 (left). I_{R} can be calculated via [Lik86]

$$I_{\mathrm{R}} = \frac{4}{\pi\sqrt{\beta_{\mathrm{C}}}} I_{\mathrm{c}} \quad , \tag{2.17}$$

with β_{C} being the dimensionless Stewart-McCumber parameter, that is used to quantitatively distinguish between both junction types. It is given by

$$\beta_{\mathrm{C}} = \frac{2\pi}{\Phi_0} I_{\mathrm{c}} R^2 C \tag{2.18}$$

with $\beta_{\mathrm{C}} \gg 1$ corresponding to a strongly underdamped junction, whereas $\beta_{\mathrm{C}} \ll 1$ represents a strongly overdamped junction. The junctions developed and produced

within the scope of this thesis aim to be overdamped, which is why we take a closer look on the time-averaged voltage for $I > I_c$ in the case of $\beta_C \ll 1$. Neglecting the noise in equation 2.15, as well as assuming the resistance to be linear below and above the gap voltage V_g, i.e. $R(V) = R$, the time-averaged voltage can be derived to [Cla04]

$$\langle V(t) \rangle = I_c R \sqrt{\left(\frac{I}{I_c}\right)^2 - 1} \quad \text{for} \quad \frac{I}{I_c} > 1 \quad . \tag{2.19}$$

This equation will be crucial to determine the voltage drop of a dc-SQUID, as its derivation is analogous to that of a single junction, which will be covered in the next section.

2.2 dc-SQUIDs

We have now covered the theoretical framework necessary to understand the working principle of a dc-SQUID, which consists of a superconducting ring intersected by two identical Josephson junctions with critical Josephson currents I_c, as depicted in figure 2.7. Both junctions are shunted with shunt resistors R_s to avoid hysteretic behavior in the respective IVCs. If the SQUID is biased with a bias current I_b, it is possible to convert small flux variations inside the loop into a measurable voltage change. dc-SQUIDs are, therefore, used as highly sensitive flux-to-voltage transducers.

2.2.1 Zero Voltage State

In order to fully understand the working principle of a dc-SQUID it is again necessary to first cover the zero voltage stage as we did for a single junction. The parallel connection of the two junctions allows the bias current with identical critical currents, i.e. $I_{c,1} = I_{c,2} = I_c$ to split into two supercurrents I_{s1}, I_{s2}. Here we assume $I_b < 2I_c$ to ensure that no voltage drop across both junctions occurs ($V_s = 0$). Applying Kirchhoff's law we then obtain the expression

$$I_b = I_s = I_c \sin \varphi_1 + I_c \sin \varphi_2 = 2I_c \cos\left(\frac{\varphi_1 - \varphi_2}{2}\right) \sin\left(\frac{\varphi_1 + \varphi_2}{2}\right) \quad . \tag{2.20}$$

In chapter 2.1.2 we concluded that a magnetic flux Φ causes the supercurrent to modulate with Φ_0. A dc-SQUID can be considered as a single junction with a much larger effective area A_{eff} (loop area), that could be penetrated vy an external magnetic flux. It is, therefore, reasonable to expect a similar behavior for a dc-SQUID.

The same approach as with a single junction is used to determine the flux depen-
dence of the total supercurrent, where a closed loop integral is performed around the
SQUID loop. The calculation leads to the relation [Gro16]

$$\varphi_2 - \varphi_1 = \frac{2\pi\Phi}{\Phi_0} \quad , \tag{2.21}$$

which can be directly inserted into equation 2.20 to obtain

$$I_\mathrm{s} = 2I_\mathrm{c} \cos\left(\pi\frac{\Phi}{\Phi_0}\right) \sin\left(\varphi_1 + \pi\frac{\Phi}{\Phi_0}\right) \quad . \tag{2.22}$$

In the most general case, however, one needs to take into account the inductance
L_s of the SQUID loop and, therefore, a circulating current $I_\mathrm{cir} = (I_\mathrm{s1} - I_\mathrm{s2})/2$ that
induces the additional flux $\Phi_\mathrm{cir} = L_\mathrm{s}I_\mathrm{cir}$. With the external flux Φ_e we can thus write
for the total flux

$$\Phi = \Phi_\mathrm{e} + \Phi_\mathrm{cir} \tag{2.23}$$

$$= \Phi_\mathrm{e} - L_\mathrm{s}I_\mathrm{c} \sin\left(\pi\frac{\Phi}{\Phi_0}\right) \cos\left(\varphi_1 + \pi\frac{\Phi}{\Phi_0}\right) \tag{2.24}$$

$$= \Phi_\mathrm{e} - \frac{1}{2}\beta_L\Phi_0 \sin\left(\pi\frac{\Phi}{\Phi_0}\right) \cos\left(\varphi_1 + \pi\frac{\Phi}{\Phi_0}\right) \quad . \tag{2.25}$$

Here, we introduced the dimensionless screening parameter $\beta_\mathrm{L} = 2L_\mathrm{s}I_\mathrm{c}/\Phi_0$, which
relates the maximum possible flux $\Phi_\mathrm{cir}^\mathrm{max} = L_\mathrm{s}I_\mathrm{cir}^\mathrm{max} = L_\mathrm{s}I_\mathrm{c}$ produced by screening
currents to $\Phi_0/2$. This quantity describes the influence the screening currents have
on the total flux Φ, which in turn affects I_s in equation 2.22. We will now simplify the
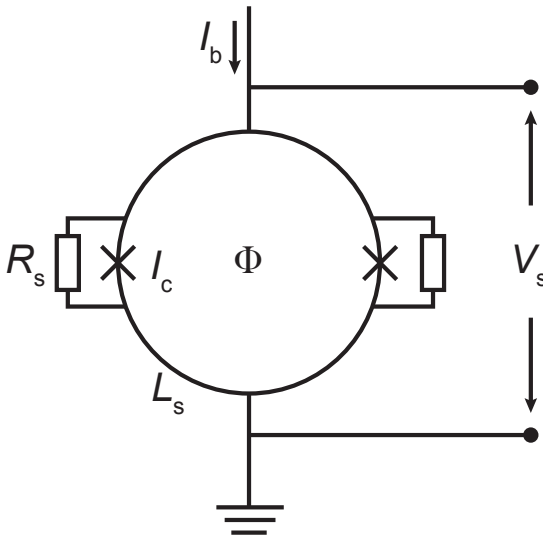

Figure 2.7: Schematic circuit di-
agram of a shunted dc-SQUID.
A superconducting loop with in-
ductance L_s is interrupted by
two Josephson junctions such that
they form a parallel connection.
With bias current is I_b and exter-
nal magnetic flux Φ. To avoid hys-
teresis effects, shunt resistors R_s
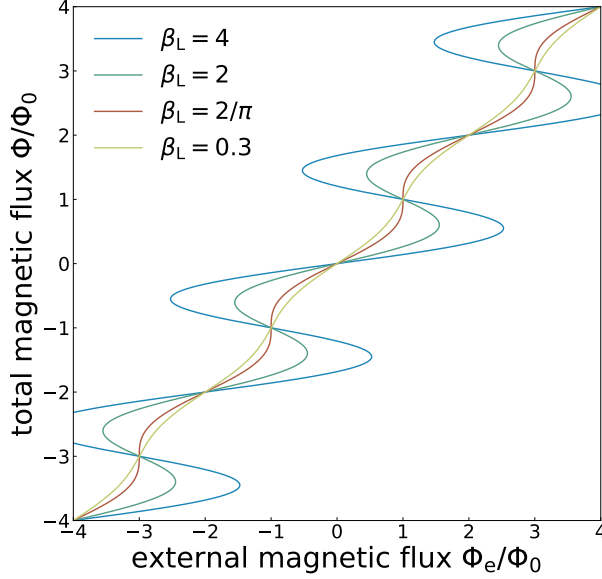are connected in parallel to each
junction.

Figure 2.8: Normalized flux Φ modulated by the external flux Φ_e. The amplitude of the modulation depends on the screening parameter β_L, where $\Phi(\Phi_e)$ remains a single-valued function for $\beta_L \leq 2/\pi$.

expression above by considering the limiting case for small currents, i.e. $I_s \ll 2I_c$. This condition implies that $\sin \varphi_1 \approx -\sin \varphi_2$ and thus $\varphi_1 \approx -\varphi_2$, leading to a vanishing argument $\varphi_1 + \pi\Phi/\Phi_0 \approx 0$ in the cosine resulting to

$$\Phi = \Phi_e - \frac{1}{2}\beta_L \Phi_0 \sin\left(\pi\frac{\Phi}{\Phi_0}\right) \quad . \tag{2.26}$$

Figure 2.8 showcases this relation for several values of β_L. High values $(\beta_L > 2/\pi)$ correspond to hysteretic characteristics, meaning there can be multiple values of total flux Φ for the same applied flux Φ_e. For practical dc-SQUIDs, it is, therefore, desirable to avoid this ambiguous behavior. The intersections of each curve represents the case for $\Phi = n\Phi_0$, such that the screening currents vanish and the total flux equals the external flux ($\Phi = \Phi_e$). This is to be expected as the flux in a superconducting ring needs to be quantized (see equation 2.2). Consequently, the SQUID tries to maintain the total flux at integer values of Φ_0 for the limiting case of $\beta_L \gg 1$, where Φ_{cir} dominates over any applied flux. This compensation is visualized by the strong modulation for high β_L in figure 2.8, where a wide range of Φ_e values remain in the proximity of $n\Phi$. The other limiting case, i.e. $\beta_L \ll 1$, allows us to neglect the circulating currents such that we can write $\Phi \approx \Phi_e$. From equation 2.22 we then obtain the maximum possible supercurrent

$$I_s^m(\Phi_e) = 2I_c \left|\cos\left(\pi\frac{\Phi_e}{\Phi_0}\right)\right| \quad . \tag{2.27}$$

The modulation of this current quickly diminishes for increasing β_{L}, as was derived in [Cla04] to

$$\frac{\Delta I_{\mathrm{s}}^{\mathrm{m}}(\Phi_{\mathrm{e}})}{2I_{\mathrm{c}}} \approx 1 - \frac{2\Phi_{\mathrm{e}}}{\Phi_0 \beta_{\mathrm{L}}} \quad . \tag{2.28}$$

For the SQUIDs produced within the scope of this thesis, values of $\beta_{\mathrm{L}} \approx 1$ were cosidered optimal to minimize resonant behavior without reducing the SQUID inductance L_{s} too much.

2.2.2   Voltage State

To utilize dc-SQUIDs as sensitive magnetometers, it is necessary to operate them in the voltage state by applying a large enough bias current I_{b}, such that $I_{\mathrm{b}} > 2I_{\mathrm{c}}$. In the case of negligible screening ($\beta_{\mathrm{L}} \ll 1, \Phi \approx \Phi_{\mathrm{e}}$) and strong damping ($\beta_{\mathrm{C}} \ll 1$), i.e. by chosing a small junction capacitance C and SQUID inductance L_{s}, it is possible to derive the flux dependence of the resulting voltage drop across the SQUID. Following the RCSJ model, we are only left with the supercurrent I_{s} and the resistive current I_{n}, such that by using equation 2.22 we can write for the bias current

$$I_{\mathrm{b}} = 2I_{\mathrm{c}} \cos\left(\pi \frac{\Phi_{\mathrm{e}}}{\Phi_0}\right) \sin\left(\varphi_1 + \pi \frac{\Phi_{\mathrm{e}}}{\Phi_0}\right) + 2\frac{V_{\mathrm{s}}}{R} \quad , \tag{2.29}$$

where we again assumed identical junctions, each shunted by a small shunt resistor $R_{\mathrm{s}} \ll R_{\mathrm{n}}$. Here R_{n} denotes the normal resistance of a single, unshunted junction. Therefore, the total normal resistance R for each branch of the SQUID is approximately $R \approx R_{\mathrm{s}}$. Additionally, we can define the phase $\varphi = \varphi_1 + \pi\Phi/\Phi_0$ and with the maximum supercurrent from equation 2.27 we obtain a current-phase relation that resembles that of a single junction:

$$I_{\mathrm{b}} = I_{\mathrm{s}}^{\mathrm{m}}(\Phi_{\mathrm{e}}) \sin(\varphi) + \frac{2}{R_{\mathrm{s}}} \frac{\Phi_0}{2\pi} \frac{\partial\varphi}{\partial t} \quad . \tag{2.30}$$

This equivalence of a dc-SQUID and a single junction underlines the above-mentioned fact that the SQUID loop represents a single Josephson contact that provides a larger effective area external fields can penetrate. It is therefore possible to derive the voltage drop across the SQUID in the same manner as in subsection 2.1.3. With the critical current $I_{\mathrm{s}}^{\mathrm{m}}(\Phi_{\mathrm{e}})$ being flux-dependent with a modulation period of Φ_0, we can
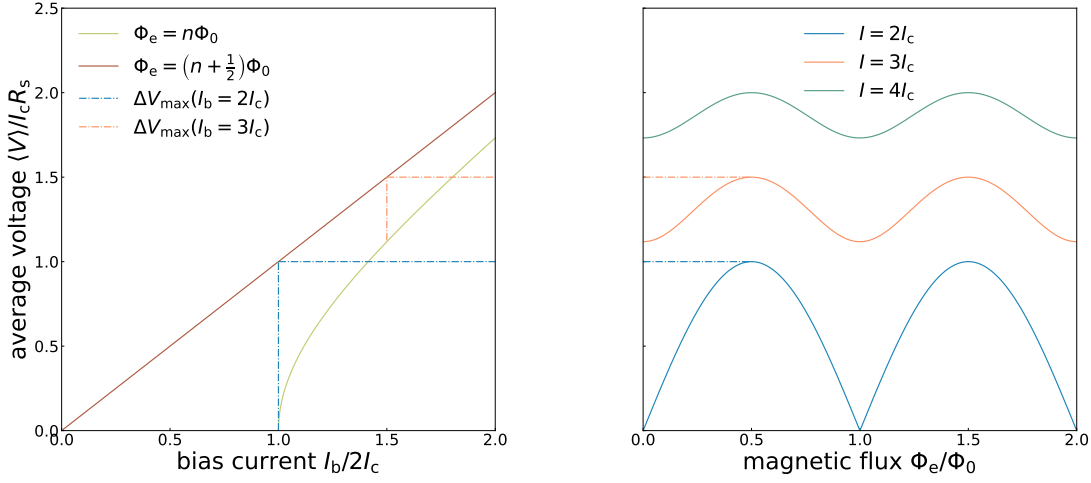
Figure 2.9: Left: IV-characteristics for the total flux $\Phi \approx \Phi_e$ being an integer and half integer number of flux quanta, given that $\beta_C \ll 1$ and $\beta_L \ll 1$. The maximum voltage swing ΔV_{max} is approximately given at $I_b \approx 2I_c$ and corresponds to $I_c R_s$ for a resistively shunted dc-SQUID. Right: The projection of equation 2.31 onto the $V\Phi$-plane shows the flux dependence of the voltage at the bias current values $I_b = 2I_c$, $I_b = 3I_c$ and $I_b = 4I_c$. The amplitude of the modulation decreases for increasing I_b.

compare to equation 2.19 and obtain for the time averaged voltage [Cla04]

$$\langle V(t) \rangle = \frac{R_s}{2} \sqrt{I_b^2 - I_s^m(\Phi_e)^2} \tag{2.31}$$

$$= I_c R_s \sqrt{\left(\frac{I_b}{2I_c}\right)^2 - \left[\cos\left(\pi \frac{\Phi_e}{\Phi_0}\right)\right]^2} \quad . \tag{2.32}$$

Evidently, both the critical current and the voltage are flux dependent and are modulated by Φ_0. Figure 2.9 (left) showcases this behavior by considering the case for the minimum and maximum critical current, i.e. for $\Phi_e = n\Phi_0$ and $\Phi_e = (n+1/2)\Phi_0$, with $n \in \mathbb{Z}$. The current-voltage-characteristics at these flux values are particularly interesting, as they can be used to extract crucial SQUID parameters like the voltage swing ΔV_{max}. This property describes how the voltage varies with the applied flux Φ_e, at a given current I_b. It is maximal at $I_b \approx 2I_c$, as depicted in figure 2.9 (right).

It is, however, important to note that equation 2.31 doesn't hold for practical SQUIDs, as they are typically not fabricated to fulfill the limiting case of $\beta_C \ll 1$ and $\beta_L \ll 1$. With few adjustments, the conclusions reached here will nevertheless

be applicable to practical SQUIDS.

2.2.3   Optimal Parameters

Negligible screening is not feasible, as it would require an extremely small SQUID inductance L_s, which in turn deteriorates the sensitivity to magnetic fields. The main reason to construct a dc-SQUID was to obtain a highly sensitive magnetometer by creating a large area for magnetic fields to penetrate. Also, the fabrication process doesn't allow to produce an arbitrarily small junction capacitance C. The parameter β_C will, therefore, reach a lower limit as well, since also decreasing R_s too much reduces the voltage swing ΔV_max and increases the energy sensitivity $\epsilon(f)$, as we will see in subsection 2.2.4. Taking into account displacement and fluctuation currents, the current and voltage expressions for the dc-SQUID become analytically unsolvable and therefore have to be solved numerically. In [Tes77] such numerical simulations lead to optimal values of $\beta_\mathrm{C} \approx 1$ and $\beta_\mathrm{L} \approx 1$ to minimize the energy sensitivity.

To further fine-tune the SQUID parameters, e.g. loop inductance and critical current, it is essential to look at how dc-SQUIDs are typically operated to achieve the highest possible flux sensitivity. Here, we distinguish between a current and a voltage bias, where the former was assumed in figure 2.9. Maximizing sensitivity in this mode is done by keeping the flux constant through a feedback loop at the steepest point in the $V\Phi$-curve, which is referred to as the working point. This allows for the largest possible voltage change ΔV at a given flux change $\Delta \Phi$. Similarly, at a voltage bias the working point (WP) will mark the steepest point in the $I\Phi$-curve. To quantify this, we introduce the transfer coefficients at the working point

$$V_\Phi \equiv \left|\frac{\partial V}{\partial \Phi}\right|_\mathrm{WP} \tag{2.33}$$

$$I_\Phi \equiv \left|\frac{\partial I}{\partial \Phi}\right|_\mathrm{WP} \quad . \tag{2.34}$$

As mentioned above, at $I_\mathrm{b} \approx 2I_\mathrm{c}$ (current bias) the amplitude of the voltage modulation is maximal. This is modified for practical SQUIDs, where thermal fluctuations can't be neglected. The resulting thermal current I_th causes a rounding of the edge at $I_\mathrm{b} = 2I_\mathrm{c}$ (figure 2.9 (left)), thereby reducing ΔV_max and V_Φ [Iva68]. To minimize this effect, numerical simulations were made that lead to the condition [Cla88]

$$\frac{I_\mathrm{c}}{5} \geq I_\mathrm{th} \equiv \frac{2\pi k_\mathrm{B} T}{\Phi_0} \quad . \tag{2.35}$$

A lower bound for I_c at $T = 4.2\,\text{K}$ will, therefore, be approximately $1\,\mu\text{A}$. This effect shifts the current $I_{\text{b,max}}$, at which the voltage swing is maximal, according to [Dru96b] by a temperature correction factor leading to

$$I_{\text{b,max}} \approx 2I_c(1 - \sqrt{\Gamma/\pi}) \quad , \tag{2.36}$$

where Γ is defined as $\Gamma = I_{\text{th}}/I_c$. Lastly, the thermal current can also be used to set an upper limit to the SQUID inductance. We can define a thermal inductance $L_{\text{th}} = \Phi_0/(2I_{\text{th}})$ for the thermal current inducing half a flux quantum. This should be significantly larger than the SQUID inductance L_s to minimize the impact of these thermal fluctuations. Again, simulations provide a constraint for optimization, giving the relation [Cla88]

$$5L_s \leq L_{\text{th}} \equiv \frac{\Phi_0}{2I_{\text{th}}} = \frac{{\Phi_0}^2}{4\pi k_{\text{B}}T} \quad . \tag{2.37}$$

For $T = 4.2\,\text{K}$ we would obtain $L_s \leq 1\,\text{nH}$, which is typically fulfilled for practical dc-SQUIDs.

2.2.4 Noise

The above-mentioned energy sensitivity, also called spectral noise energy density or energy resolution, is defined as the flux noise per SQUID inductance L_s and is typically expressed through a power spectral density as

$$\epsilon(f) = \frac{S_\Phi(f)}{2L_s} \quad . \tag{2.38}$$

This conveniently allows to compare noise properties from SQUIDs with different loop inductances [FS24]. The flux noise power spectral density $S_\Phi(f)$ is typically calculated from the voltage noise using the transfer coefficient introduced above:

$$S_\Phi(f) = \frac{S_V(f)}{V_\Phi^2} \quad . \tag{2.39}$$

The flux noise in SQUIDs is typically separated into a frequency-independent white noise at higher frequencies and a low frequency $1/f$-noise component [Koc07]. To derive an expression for $S_V(f)$ we consider the white noise only, limiting ourselves to higher frequencies to avoid any significant influence of $1/f$-noise. For this we need to distinguish between the noise stemming from the bias current and the circulating current inside the SQUID-loop. The former is affected by the total resistance of the

SQUID which corresponds to $R_s/2$ for $I \gg I_{b,max}$ and to the dynamic resistance $R_{dyn} = \partial V/\partial I$ for operation at the working point. The circulating current, however, is affected by two resistances in series, i.e. $2R_s$. By taking into account noise inducing resonances due to the simulated optimal values of $\beta_C \approx 1$ and $\beta_L \approx 1$ that exhibit hysteretic behavior, both noise currents can be used to obtain the voltage noise given by [Tes77], [Bru82]

$$S_V(f) = \frac{4k_B T}{R_s} \left[2R_{dyn}^2 + \frac{L_s^2 V_\Phi^2}{2} \right] \quad . \tag{2.40}$$

Here, we used the approximation $V_\Phi \approx I_c R_s/(\Phi_0/2) \approx R_s/L_s$ valid for $\beta_L \approx 1$. This approximation leads to the expression $R_{dyn} \approx \sqrt{2}R_s$ for the dynamical resistance, which can be used to rewrite equation 2.40 to

$$S_V(f) = 18k_B T R_s \quad . \tag{2.41}$$

Inserting this into equations 2.39 and 2.38 leads to the expression

$$\epsilon(f) \approx 16k_B T \sqrt{\frac{L_s C}{\beta_C}} \approx 16k_B T \sqrt{L_s C} \quad \text{for} \quad \beta_C \approx 1 \quad . \tag{2.42}$$

For a moderately damped dc-SQUID ($\beta_C \approx 1$) at a temperature $T = 100\,\text{mK}$ and with a suitably small inductance $L_s = 100\,\text{pH}$ we would, therefore, obtain a theoretical value of $\epsilon \approx 0.32\,\text{h}$.

Finally, we will look at the total flux noise spectrum by considering the $1/f$ component, which is added to the above derived white noise dominating in the low frequency regime. The origin of this component is still unclear [Kem16]. It is parameterized by a power density at $1\,\text{Hz}$, giving a total noise power density of

$$S_\Phi(f) = S_{\Phi,w} + \frac{S_{\Phi,1/f}(1\,\text{Hz})}{f^\alpha} \quad , \tag{2.43}$$

with $S_{\Phi,w}$ being the white noise component and α ranging from 0.5 to 1 [Dru11], which can be determined by experiment.

2.2.5   Parasitic Resonances

We have seen that optimizing properties of dc-SQUIDs requires careful fine-tuning of various parameters to ensure high sensitivity and low noise at the same time. Another
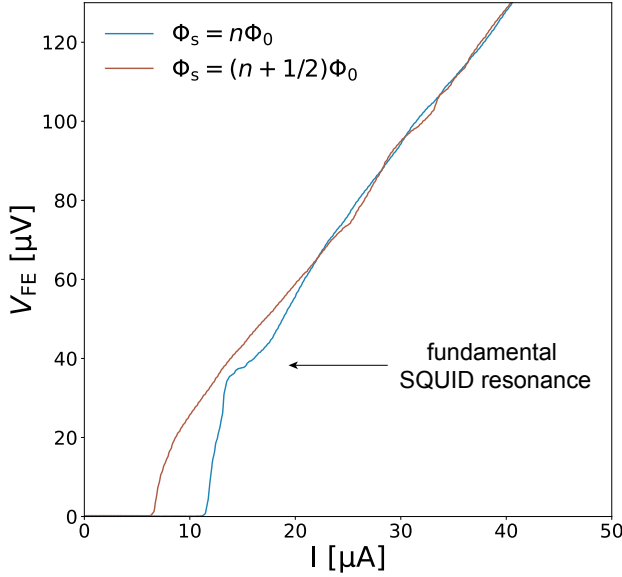
Figure 2.10: Measured IV-characteristic of a dc-SQUID developed within the scope of this thesis. The first current step at $V_s \approx 40\,\mu V$ corresponds to the fundamental SQUID resonance for $L_s = 119\,\mathrm{pH}$ and $C = 0.95\,\mathrm{pF}$.

constraint in this regard involves the presence of resonances in the system that we need to take into account. As discussed in subsection 2.1.3, a Josephson contact also represents a parallel plate capacitor with capacitance C. Here we take into account the total capacitance of $C/2$, due to the series connection of the two junctions within the SQUID loop. The SQUID with its loop inductance L_s will, therefore, form an LC resonator that can be excited if the Josephson currents oscillate with the resonance frequency $f_{L_sC} = 1/(2\pi\sqrt{L_sC/2})$. This is fulfilled for the condition

$$\frac{V_s}{\Phi_0} = \frac{1}{2\pi\sqrt{L_sC/2}} \quad , \tag{2.44}$$

where V_s denotes the voltage drop across the SQUID that is associated with the Josephson frequency $f_J = V_s/\Phi_0$ resulting from the ac Josephson effect. With optimal β_C and β_L values the voltage corresponding to this resonance frequency will move towards the vicinity of the working point, thus becoming relevant for the SQUID's performance. This so-called *fundamental SQUID resonance* negatively affects the operation range by manifesting itself through a current step in the IVC, as shown in figure 2.10. As a result, the IV curves for integer and half integer flux quanta intersect as a result multiple times, due to higher harmonics of the resonance causing additional current steps [Cla04]. The voltage swing ΔV and consequently V_Φ are limited by this resonance, which favors the choice of small values for L_s and C.

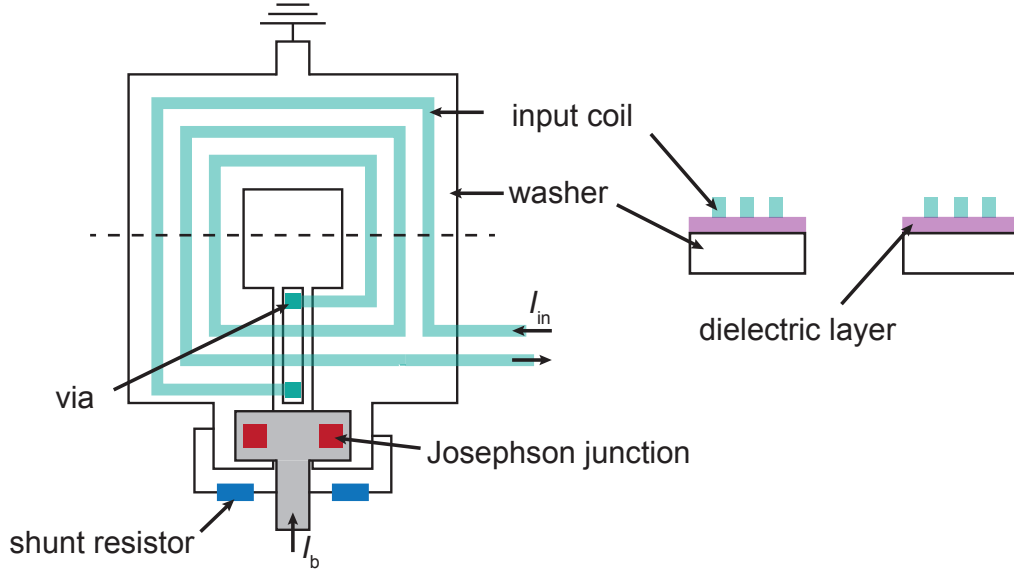Resonance inducing structures are, however, necessary for practical reasons. Those

Figure 3.1: Schematic drawing of a typical planar thin-film dc-SQUID. The SQUID
loop is realized as a square washer-geometry interrupted by a narrow slit, only con-
nected at the junction area. A thin insulating layer separates the washer from the
planar multi-turn input coil above. Left: View from the top. Right: Cross section
marked by the dashed line.

coupling can be achieved by the commonly used square *washer*-geometry with a
planar input coil [Jay81], as shown in figure 3.1.

Here, the SQUID loop is represented by the washer, whereas each turn of the input
coil is located on top of it to maximize the coupling between both coils. A cross
section of this setup is depicted in figure 3.1 (right), showing the insulating dielectric
layer separating each coil. The washer is intersected by a slit, which starts at the
square hole in the middle and ends at the remotely situated junction area that
connects each side of the loop. The total inductance of the SQUID loop can be
calculated by adding the dominating washer hole inductance L_h, the slit inductance
$L_\mathrm{sl} \approx 0.3\,\mathrm{pH/\mu m}$ given for small slit dimensions and the much smaller parasitic
inductance L_j associated with the junction area, giving [Ket91]

$$L_\mathrm{s} = L_\mathrm{h} + L_\mathrm{sl} + L_\mathrm{j} \quad . \tag{3.3}$$

The latter is referred to as parasitic due to it's position outside of the input coil,
thus not contributing to the coupling. By neglecting L_sl and L_j, we can approximate
the washer inductance in the limit of $d \ll w$ to $L_\mathrm{s} \approx L_\mathrm{h} \approx 1.25\mu_0 d$, where d and w
are the inner and outer side lengths, respectively [Jay81]. This is a reasonable result
considering that the supercurrent will only flow along the inner edge of the washer

[Ket82], thereby being independent of the outer side length w. The effective area A_{eff} of the SQUID loop has been calculated to $A_{\text{eff}} \approx dw$ [Ket85], showing that this geometry allows for high sensitivity while keeping the SQUID inductance small. The input coil inductance on the other hand can be approximated by $L_{\text{i}} = L_{\text{str}} + n^2 L_{\text{s}}$, where L_{str} is the stripline inductance (see section 5.2) and n is the number of input coil turns [Jay81]. The dc-SQUID designs used in this working group, however, are too complex to provide such analytical expressions and therefore need to be calculated numerically using simulation softwares such as *InductEX*[1].

3.1.1   Gradiometer

The high flux sensitivity of a SQUID makes it prone to detect unwanted magnetic bias fields and/or gradients that may be present during its operation. Typical SQUIDs are, therefore, built in a gradiometric design to counteract this effect [Ket78]. A first order gradiometer consists of two identical conducting loops connected in series or parallel, with opposing orientation as shown in figure 3.2 (left, middle). Under the presence of a homogeneous bias field $\mathbf{B}$ in x-direction (perpendicular to the gradiometer plane), this configuration produces a zero net current after a field change ΔB_x, due to the opposing currents induced in each turn. To also achieve the same effect for a field gradient $\partial \mathbf{B}/\partial z$ or $\partial \mathbf{B}/\partial y$, a second order gradiometer composed of four loops in series or parallel is required, see figure 3.2 (right), where only the currents induced in the upper loops are drawn for the sake of clarity. In order to incorporate this into a practical SQUID, the input coil and the SQUID loop will consist of four serial and parallel turns, respectively. This configuration enables to combine a small SQUID inductance with a large input coil inductance while maintaining a strong coupling between the two, as each turn of both coils can be produced with similar dimensions. The low SQUID inductance results from the reciprocal summation over each loop inductance L_{l} due to the parallel connection, giving

$$L_{\text{s}} = \frac{L_{\text{l}}}{4} \quad . \tag{3.4}$$

Whereas a serial gradiometer gives

$$L_{\text{i}} = 4L_{\text{l}} \tag{3.5}$$

for the input coil, provided it consists of only one turn. This gradiometric setup allows for adapting the input coil to the pickup coil of an MMC by choosing a large

---

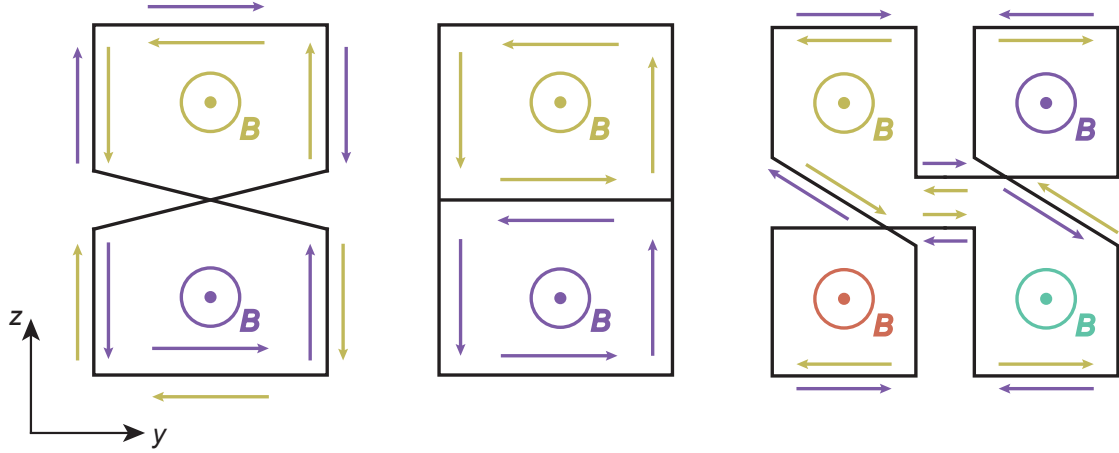[1]SUNMagnetics, 15 De Beer Rd, Stellenbosch Central, Stellenbosch, 7600, South Africa

Figure 3.2: Schematic examples of a gradiometric dc-SQUID configuration threaded by a homogeneous magnetic field $\mathbf{B}$. A first order gradiometer can be realized by either connecting two loops in series (left) or in parallel (middle). A magnetic field change ΔB_{x} induces two opposing currents that cancel each other out. Right: Second order gradiometer consisting of four loops connected in series. This geometry results in a net zero current also for an applied field gradient $\partial \mathbf{B}/\partial z$. For the sake of clarity, the currens induced in the two bottom loops are omitted.

enough inductance L_{i}, which will be discussed in chapter 4.

3.2   Operation of a dc-SQUID

The SQUIDs developed within the scope of this thesis are produced in the institute's cleanroom and then tested both in a single- and a two-stage setup (see subsection 3.2.2). The measurements described in chapter 5 are carried out at either $T = 4.2\,\mathrm{K}$ in a liquid helium transport vessel or in a dilution cryostat BF-LD250 from BlueFors[2] with a base temperature of $T = 10\,\mathrm{mK}$. The former submerges the SQUIDs in liquid helium via a dipstick, which provides a sample holder for PCBs. The SQUIDs are glued onto those PCBs and are electrically connected to them via aluminum bond wires, by utilizing the bond pads shown in figure 4.4. The sample holder is equipped with both a superconducting (niobium) and a soft-magnetic Cryoperm shield to suppress external magnetic fields. The read-out is done by a broadband SQUID electronics of the type XXF-1 (see subsection 3.2.1) to both supply the necessary bias and ramp current signals to the SQUID as well to provide the FLL feedback. The SQUID electronics is controlled via software and the voltage output observed

---

[2]BlueFors Cryogenics Oy, Arinatie, 00370 Helsinki, Finnland

on a Keysight InfiniiVision[3] oscilloscope.

3.2.1 Flux-Locked Loop

We have seen in section 2.2.2 that the periodic $V\Phi$-characteristic provides an approximately linear dependence at $\Phi = (2n + 1)\Phi_0/4$, which only holds for $\Delta\Phi \approx \Phi_0/4$. This restricts the dynamic range greatly, as the linearity vanishes for larger flux changes and for $\Delta\Phi > \Phi_0/2$ the voltage even becomes ambiguous.

The standard readout method involves a flux feedback circuit to maintain the operation at the working point independently of the flux [Dru02]. This so-called flux-locked loop (FLL) readout technique first amplifies the output signal of the SQUID V_s with a differential amplifier operated at room temperature, where the voltage V_b corresponding to the working point is provided by a voltage source on the second amplifier input. This voltage compensation at the working point ensures that only variations $\Delta V = V_\mathrm{s} - V_\mathrm{b}$ that correspond to the flux change $\Delta\Phi$ are amplified. The signal is then fed into an integrator, which integrates it over time and thus creates a changing output voltage V_out. By connecting a feedback resistance R_fb to the output circuit, a feedback current I_fb is generated that flows to a feedback coil with inductance L_fb. This coil is coupled to the SQUID analogous to the input coil (see chapter 4), but with the opposite orientation. A compensation flux $-\Delta\Phi$ is generated until the initial flux change is fully canceled out, i.e. $V_\mathrm{s} - V_\mathrm{b} \to 0$. The integrator will, therefore, approach a constant value due to the vanishing voltage at the input circuit. This voltage signal is proportional to the current that is needed to completely compensate for the input signal $\Delta\Phi$, leading to the relation

$$V_\mathrm{out} = \frac{R_\mathrm{fb}}{M_\mathrm{fb}}\Delta\Phi \quad . \tag{3.6}$$

A schematic for this readout process is shown in figure 3.3. With this setup the SQUID is used as a null-detector that allows for the linearization of the quantity of interest, while also providing a large dynamic range. A state-of-the-art, low-noise SQUID readout electronics by the company Magnicon[4] of the type XXF-1, which is used in this working group, provides the necessary current and voltage sources, as well as the room temperature amplifiers within the FLL circuit described above. The amplifier of this SQUID electronics exhibits an intrinsic voltage noise of $\sqrt{S_{V,\mathrm{el}}} \approx 0.33\,\mathrm{nV}/\sqrt{\mathrm{Hz}}$ and intrinsic current noise of $\sqrt{S_{I,\mathrm{el}}} \approx 2.6\,\mathrm{pA}/\sqrt{\mathrm{Hz}}$ [Dru06]. The included current source for the feedback coil couples current noise into the SQUID. In the work of [Kaa20], this contribution was determined to $\sqrt{S_{I,\Phi}} = 2.4\,\mathrm{pA}/\sqrt{\mathrm{Hz}}$ for

---

[3]Keysight Technologies Deutschland GmbH, Herrenberger Straße 130, 71034 Böblingen
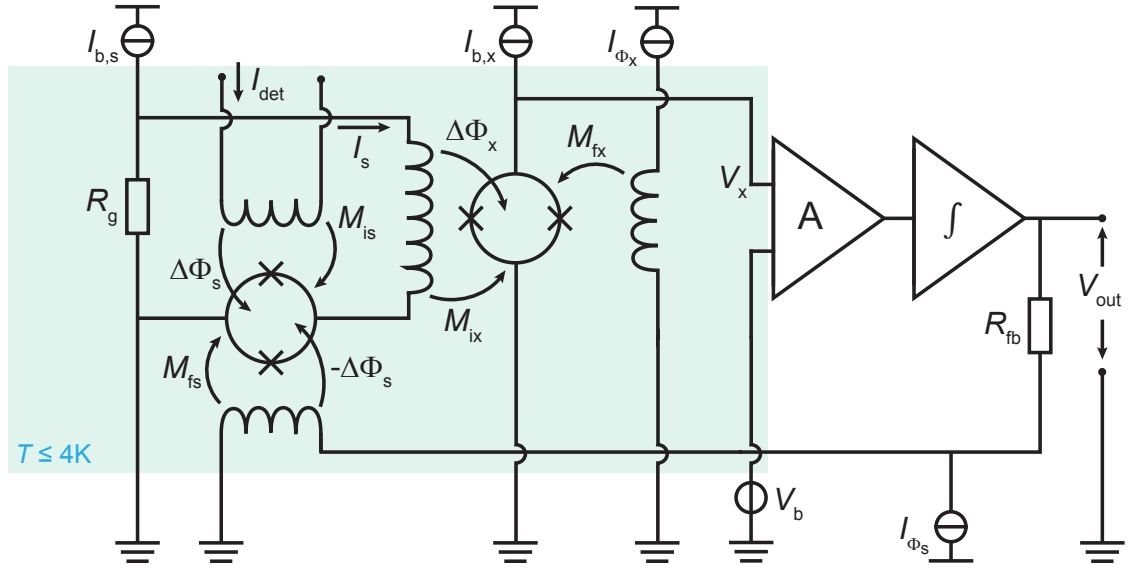[4]Magnicon GmbH, Barkhausenweg 11, 22339 Hamburg

Figure 3.4: Schematic circuit diagram of a two-stage dc-SQUID readout. The first stage consisting of the detector SQUID is connected in parallel with a gain resistor R_{g}. The detector signal I_{det} induces a current change ΔI_{s} in the front-end and, therefore, a flux change $\Delta\Phi_{\mathrm{x}}$ in the second stage SQUID, which acts as a low temperature preamplifier. In FLL mode, the signal will be fed back to compensate for the initial flux change $\Delta\Phi_{\mathrm{s}}$, thereby linearizing the detector signal. Choosing an N-SQUID series array amplifies the voltage swing and transfer coefficient, thus significantly reducing the overall apparent flux noise in the detector SQUID.

an upper limit for the flux gain, however, it should be chosen as large as possible to reduce the apparent flux noise of the Front-End SQUID. An optimal flux gain has been calculated to $G_{\Phi} \approx \pi$, corresponding to $\Delta\Phi_{\mathrm{x}} \approx \Phi_0/2$ [Dru96a].

The two-stage setup contributes additional noise sources to equation 3.7, namely the gain resistor and the amplifier SQUID. However, the resulting conversion to the flux Φ_{s} of the front-end SQUID significantly reduces the influence of the room temperature amplifier, which in turn strongly improves the overall signal to noise ratio. The total apparent flux noise of the Front-End then reads [Dru96a]

$$S_{\Phi_{\mathrm{s}},\mathrm{SQ}} = S_{\Phi_{\mathrm{s}}} + \frac{4k_{\mathrm{B}}TR_{\mathrm{g}}}{G_{\Phi}^2(R_{\mathrm{g}}+R_{\mathrm{dyn}})^2}M_{\mathrm{ix}}^2 + \frac{S_{\Phi_{\mathrm{x}}}}{G_{\Phi}^2} + \frac{S_{V,\mathrm{el}}}{G_{\Phi}^2 V_{\Phi_{\mathrm{x}}}^2} + \frac{S_{I,\mathrm{el}}}{G_{\Phi}^2 I_{\Phi_{\mathrm{x}}}^2} + \frac{S_{I,\Phi_{\mathrm{x}}}M_{\mathrm{fx}}^2}{G_{\Phi}^2} \quad . \quad (3.9)$$

The second term describes the Nyquist current noise caused by the gain resistor, which becomes negligible with a voltage biased front-end SQUID where $R_{\mathrm{g}} \ll R_{\mathrm{dyn}}$. The low temperature amplifier (array), the feedback coil current source as well as the room temperature amplifier contributions are reduced by the flux gain, which can't

be chosen arbitrarily large as mentioned above. However, using a SQUID array for the second stage increases the voltage swing and thus the transfer coefficient by an N-fold, i.e. $V_{\Phi_x} = NV_{\Phi_{cell}}$, where the subscript 'cell' refers to a single array SQUID cell. Consequently, the total noise level can be further reduced by choosing a high number N of SQUID cells. Here it is noteworthy, however, that these considerations only account for the magnetic flux in a single cell, as otherwise the transfer coefficient would remain constant [Sta93, Fog93]. Using equation 2.39 we obtain for the SQUID array flux noise

$$\sqrt{S_{\Phi_x}} = \frac{\sqrt{S_{V_x}}}{V_{\Phi_x}} = \frac{\sqrt{NS_{V_{cell}}}}{NV_{\Phi_{cell}}} = \frac{1}{\sqrt{N}}\sqrt{S_{\Phi_{cell}}} \quad , \tag{3.10}$$

hence the intrinsic noise of the second stage gets reduced by a factor of $1/\sqrt{N}$ [Sta93]. This also has a consequence for the coupled energy sensitivity of the SQUID array, which is calculated by summing the array flux noise over all N cells, giving

$$\epsilon_{c,x} = N\frac{S_{\Phi_x}}{2L_{cell}k_{i,cell}^2} = \frac{S_{\Phi_{cell}}}{2L_{cell}k_{i,cell}^2} \quad . \tag{3.11}$$

Where the parameter $k_{i,cell}$ denotes the coupling of a cell with inductance L_{cell} to its respective input coil segment. Connecting N SQUIDs in series does, therefore, not affect the energy sensitivity, provided that $k_{i,cell}$ remains constant across the array. The arrays produced in this working group either contain 16 [Kem15] or 18 [Kra23] cells. Applying this to equation 3.9, we would reduce the above-mentioned contribution of the room temperature amplifier flux noise of $4.13\,\mu\Phi_0/\sqrt{Hz}$ to $0.29\,\mu\Phi_0/\sqrt{Hz}$ and $0.26\,\mu\Phi_0/\sqrt{Hz}$ for $N = 16$ and $N = 18$, respectively. Provided an optimal flux gain of $G \approx \pi$, the noise contribution would further decrease to $0.09\,\mu\Phi_0/\sqrt{Hz}$ or $0.08\,\mu\Phi_0/\sqrt{Hz}$, well below the typical noise level of a front-end SQUID.

Besides the improvement of the noise behavior, a major advantage of a two-stage setup consists of the low power dissipation produced by the front-end SQUID. As opposed to the current bias operation in a single-stage setup, the Front-End is held at a constant, low voltage, such that the dissipated power given by $P = UI$ only consists of approximately $1\,nW$ [Dru07].

3.3   Metallic Magnetic Calorimeters

Low temperature detectors used in this working group exhibit detector arrays consisting of metallic magnetic calorimeters, which are able to absorb and detect photons (X- or Gamma-rays) or heavy particles. The focus of this thesis is to improve the dc-SQUID based MMC readout, which is why we briefly cover the working principle
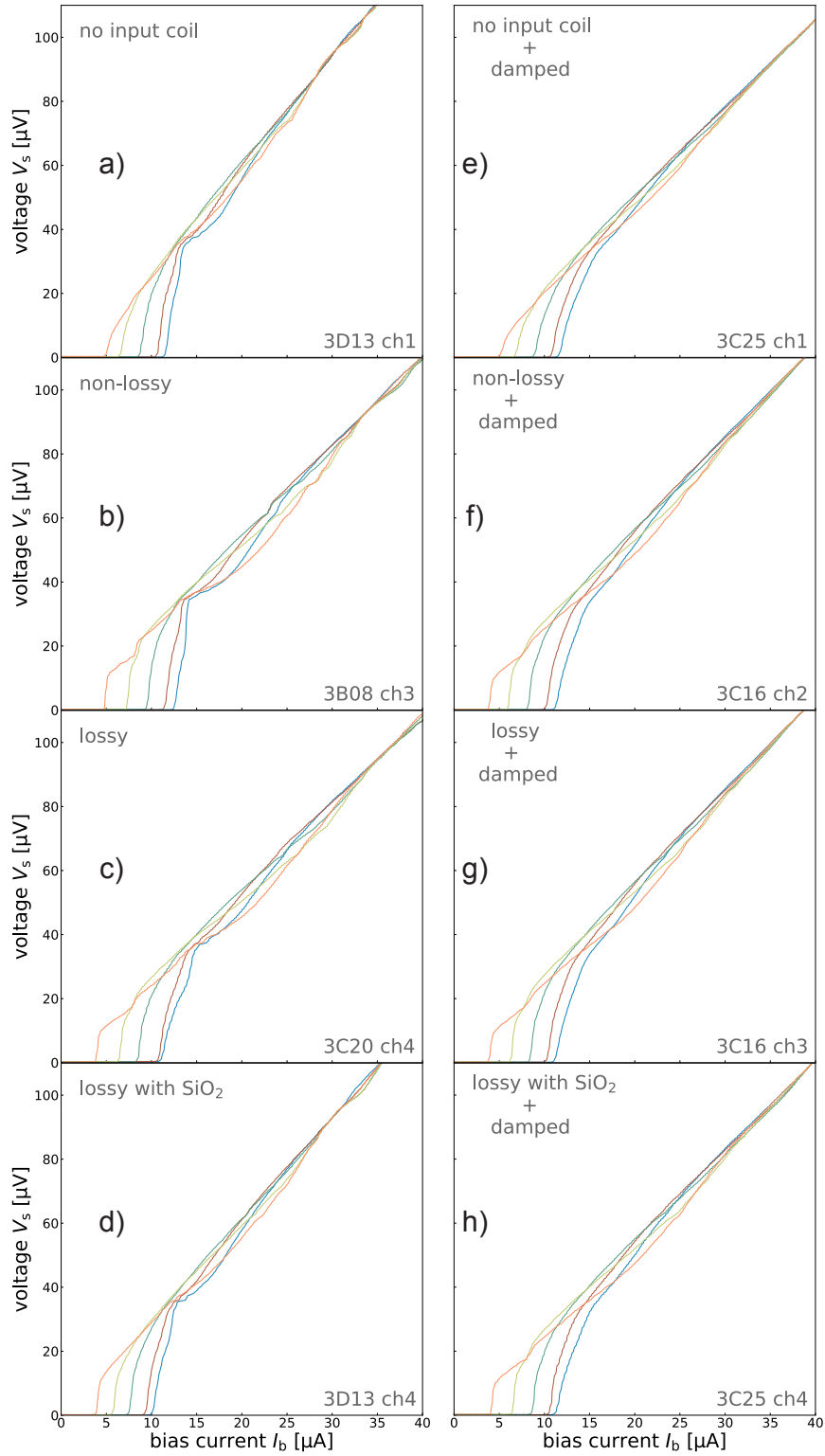
Figure 5.3: a) - d): Measured IVCs of the SQUID types presented in figure 4.4 in the same order, but without inductive damping. e) - h): The same measurement for the respective SQUID types but with inductive damping. Measured at $T = 10\,\mathrm{mK}$.

the damped and current-biased SQUIDs to be lower. Whether the various step structures apart from the large step at $40\,\mu$V can be assigned to the different microstrip and LC resonances described in subsection 2.2.5 will be the subject of the following discussion.

A second prominent step structure seen in the IVCs of figure 5.3 occurs at approximately $15\,\mu$V for the extremal curve with the smallest critical current $I_{c,1}$. This feature is absent in the IVCs of the SQUIDs without input coil (plots a) and e)) and was also not visible for the design with a single-turn input coil, which was measured alongside the SQUIDs discussed in this section. Consequently, the second turn seems to cause an additional resonance effect, which could not be identified with the resonances described in the following. It is also unclear why this artefact does not appear in plot d) of figure 5.3.

Interestingly, there are no considerable differences between the characteristics of lossy and non-lossy variants. It is, however, worth noting that the input coils were not shorted or connected to a pickup coil during the experiments described in this chapter, which might result in an altered resonance behavior. The resonance as well as the noise properties of the new SQUID design with a shorted input coil should, therefore, be investigated in future works.

C_{p}-related resonances   For the C_{p}-related resonances, we need to take into account that the SQUID loops are connected in parallel and the input coil in series. The parasitic capacitance $C_{\mathrm{p}}^{\mathrm{loop}}$ per washer loop, therefore, has to be multiplied by a factor of 4 or 1/4 respectively to obtain the total parasitic capacitance C_{p}. A theoretical value has been calculated to [Enp91, Enp92]

$$C_{\mathrm{p}}^{\mathrm{loop}} = \frac{l_{\mathrm{i},1/4} C_{\mathrm{str}}}{8} = \frac{l_{\mathrm{i},1/4}}{8} \frac{\epsilon_0 \epsilon_{\mathrm{r}} w_{\mathrm{i}} K_{\mathrm{f}}(w_{\mathrm{i}}, t_{\mathrm{i}}, h)}{h} \quad , \tag{5.4}$$

where $l_{\mathrm{i},1/4}$ denotes the input coil length on a single washer loop and C_{str} the microstrip line capacitance per unit length. The latter depends on the vacuum and relative permittivity ϵ_0 and ϵ_{r}, as well as the width of the input coil w_{i}, the fringing factor $K_{\mathrm{f}}(w_{\mathrm{i}}, t_{\mathrm{i}}, h)$ and the insulation thickness h. The fringing factor also depends on w_{i}, h and the thickness of the input coil denoted as t_{i} [Cha79]. With $h = 375\,$nm, $w_{\mathrm{i}} = 3\,\mu$m and a sputtered Nb2 layer with $t_{\mathrm{i}} = 400\,$nm we obtain the value $K_{\mathrm{f}} = 1.45$. In case of the lossy SQUID variants, the niobium thickness of the input coil was fabricated to be $t_{\mathrm{i}} = 200\,$nm, leading to $K_{\mathrm{f}} = 1.42$. This has a small effect on the resulting resonance frequencies, as they only deviate approximately $2\,\%$ from the respective frequencies obtained for the non-lossy type. For the sake of clarity, we will, therefore, only consider the non-lossy SQUID in the following discussion, which will qualitatively represent the lossy type as well.

With a fringing factor of $K_f = 1.45$, we obtain a microstrip capacitance of $C_{str} = 0.4 \, nF/m$. The input coil length per washer loop is approximately given by $l_{i,1/4} \approx l_i/4 \approx 860 \, \mu m$, with the total length of the input coil being $l_i \approx 3.44 \, mm$. Consequently, we obtain for the parasitic capacitance per washer loop $C_p^{loop} = 0.043 \, pF$. The total parasitic capacitance regarding the washer is, therefore, $C_p = 4C_p^{loop} = 0.17 \, pF$, which is still small compared to the junction capacitance $C = 0.95 \, pF$, i.e. $C_p/C \ll 2$. The influence of this parameter on the energy sensitivity should consequently be small, as explained in subsection 2.2.5. The $L_s C_p$ resonance can now be calculated to $f_{L_s C_p} = 1/(2\pi\sqrt{L_s 4 C_p^{loop}}) = 34 \, GHz$, where we used the measured SQUID loop inductance $L_s = 108 \, pH$. This corresponds to a voltage drop of $V_s = 70.2 \, \mu V$ for the condition $f_J = f_{L_s C_p}$. Mostly the plots a) through c) from figure 5.3 showcase small distinctive step-like structures around $75 \, \mu V$. These could, however, also stem from a higher harmonic of the fundamental SQUID resonance, which should be the case for the SQUID without input coil (a)), as there is no corresponding parasitic capacitance. The value of $f_{L_s C_p} = 34 \, GHz$ is well above the optimal operation frequency for a current-biased SQUID, given by $f_{op} \approx 0.3 f_c \approx 5.1 \, GHz$ ($V_s = 10.5 \, \mu V$), with $f_c = I_c R_s/\Phi_0$ [Can96] and is, therefore, not relevant in typical SQUID operation.

To discuss the $f_{L_i C_p}$ resonance we need to take the $R_x C_x$ attenuator into account. The capacitances C_x and C_p can approximately be added up to the total capacitance $C_{tot} = C_x + C_p^{loop}/4$ due to the serial connection of the input coil. The geometric input coil inductance is shielded analogously to L_s (compare equation 3.18), giving the relation $L_i' = (1 - k_{is}^2 s_s)L_i$ [Can96]. Here, the screening factor was derived to $s_s = \beta_L s_i k_{is}^2/(6 + 2\beta_L + \beta_L s_i k_{is}^2)$. The input inductance of the SQUID and pickup coil inductance of the detector also form a parallel connection, resulting in $L_{tot} = L_i' L_p/(L_i' + L_p)$. The resonance frequency then reads

$$f_{L_i C_p} \approx \frac{1}{2\pi\sqrt{C_{tot} L_{tot}}} \quad , \tag{5.5}$$

which by using our measured and calculated parameters yields $0.9 \, GHz$. The corresponding voltage drop is $V_s = 1.8 \, \mu V$, which is well below the above-mentioned operation voltage and is, therefore, not visible in the IVCs from figure 5.3. The capacitance C_x is chosen small to minimze the attributed $Q_{L_i C_p}$ value, which for an RCL parallel circuit is given by

$$Q_{L_i C_p} \approx R_x\sqrt{\frac{C_{tot}}{L_{tot}}} \approx \frac{R_x}{f_{L_i C_p} L_{tot}} \quad . \tag{5.6}$$

Evidently, C_x cannot be chosen arbitrarily small as it would shift the resonance to the vicinity of the working point. An optimal value has been found to be $Q_{L_i C_p} \approx 2$

[Can96]. The resistive componenet of the attenuator is typically dimensioned such that it corresponds to the nominal impedance Z_0 of the microstrip line in order to mitigate wave reflections occuring where the input coil leaves the SQUID loop. This impedance can be expressed as [Enp91]

$$Z_0 = \sqrt{\frac{L_{\text{str}}}{C_{\text{str}}}} \quad . \tag{5.7}$$

With the produced geometric proportions of the microstrip, the optimal value yields $R_{\text{x}} = 20.6\,\Omega$, which was chosen as the design value. Therefore, with equation 5.6 we obtain an optimal capacitance of $C_{\text{x}} = 31\,\text{pF}$. However, for this first design, the capacitance of $10\,\text{pF}$ chosen for the previous design in [Bau22] has been adapted to be on the safe side regarding the quality factor. In our case we obtain $Q \approx 1.13$, however, the corresponding resonance frequency is still small enough to consider the effect of this resonance as negligible.

We can also further neglect the C_{p}-related resonance with respect to the feedback coil, as its small design inductance of $L_{\text{f}} = 336\,\text{pH}$ leads to a resonance frequency of $f_{L_{\text{f}}C_{\text{p}}} = 77\,\text{GHz} = 160\,\text{µV}/\Phi_0$, well above f_{op}.

Microstrip line resonances   Regarding the $\lambda/2$ resonances a distinction is made whether the inpt coil or the SQUID loop act as the signal carrying line. They will consequently be referred to as the input coil or washer resonance with the resonance frequencies $f_{l_{\text{i}}}$ or $f_{l_{\text{w}}}$, respectively. These should ideally fulfill the condition $4f_{l_{\text{i}}} < f_{\text{op}} < f_{l_{\text{w}}}/4$ to mitigate their noise inducing influence at the working point [Can91]. The wave propagation velocity c_{str} depends on L_{str} and C_{str}, such that equation 2.45 becomes [Enp92]

$$f_{l_{\text{i}}} = \frac{c_{\text{str}}}{2l_{\text{i}}} = \frac{1}{2l_{\text{i}}\sqrt{L_{\text{str}}C_{\text{str}}}} \quad . \tag{5.8}$$

With the length of the input coil l_{i}, we obtain for the input coil resonance $f_{l_{\text{i}}} = 17.6\,\text{GHz} = 36.4\,\text{µV}/\Phi_0$. However, we need to include the length $l_{\text{i}}^{\text{feed}} \approx 620\,\text{µm}$ of the input coil feed lines which are also structured as a microstrip transmission line. This results in $14.9\,\text{GHz}$ and accordingly $V_{\text{s}} = 30.9\,\text{µV}$. Even though the condition $4f_{l_{\text{i}}} < f_{\text{op}}$ is not fulfilled, there are no visible step structures in the vicinity of this frequency, which suggests successful damping of this microstrip resonance. The effectiveness of the $R_{\text{x}}C_{\text{x}}$ attenuator has also been demonstrated in [Bau22], where prominent step structures at $f_{l_{\text{i}}} = 54\,\text{µV}/\Phi_0$ were eliminated entirely after adding the $R_{\text{x}}C_{\text{x}}$ component to the SQUID design with $L_{\text{i}} = 1.27\,\text{nH}$.

The washer resonance is more difficult to determine for the given SQUID loop design, as the complex washer structure surrounding the junction area affects the effective